

Preparation of Reduced Graphene Oxide Aerogel and its Application in Lithium Sulfur Battery

Jianrong Xiao^{1,*}, Zhiyun Yang¹, Hongzhe Wang², Yafang Guo¹, Zengren Tao¹

¹ College of Science, Guilin University of Technology, Guilin 541004, Guangxi Province, China

² School of Materials Science and Engineering, Science and Engineering, Southeast University, Nanjing 211189, Jiangsu Province, China

*E-mail: xjr@glut.edu.cn

Received: 31 August 2017 / Accepted: 11 October 2017 / Published: 12 November 2017

A facile method was used to prepare novel nitrogen-doped sulfur-based compound material coated with reduced-graphene-oxide aerogel NCNT/S(RGO-gel) composite. As coating layer, the material was systematically studied through X-ray diffraction, scanning electron microscopy, Fourier transform infrared spectroscopy, and electrochemical test. NCNT/S(RGO-gel) electrode showed first discharge specific capacity of 1403.7 mAh·g⁻¹ under 500 mA/g density. The material also exhibited outstanding rate capability and long-term cycle stability. Results showed that RGO-gel coated composite electrode retained its discharge specific capacity of 912.4 mAh/g after 175 cycles under 500 mA/g current density. The composite electrode presented capacity retention rate of 80%. Improved electrochemical performance was mainly ascribed to RGO-gel, which not only reduced dissolution of sulfur polymer (S_n²⁻) but also significantly improved conductivity. NCNT also served as bridge between RGO-gel layers, significantly shortening the path for lithium-ion transport. Thus, novel NCNT/S(RGO-gel) composite can act as potential positive electrode for high performance Li-S batteries.

Keywords: RGO-gel, coating layer, Li-S battery, electrochemical performance

1. INTRODUCTION

Chemical power is energy stored between super capacitors and ordinary capacitor equipment. Lithium-sulfur (Li-S) batteries are superior to ordinary commercial lithium-ion batteries; this type has capacity of 1675 mAh/g and energy density of 2600 Wh/kg[1]. Sulfur has rich reserves, low price, non-polluting trait, and other significant features that make it potentially applicable for next generation of lithium-ion batteries[2]. However, many bottlenecks still restrict commercial production of Li-S batteries[3]. First, relatively low electrochemical activity and utilization result from electronic

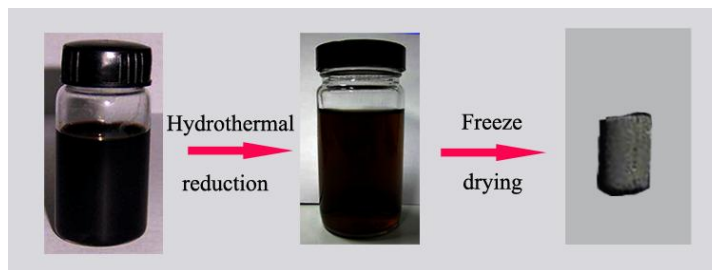
insulation of elemental sulfur (S_8) at room temperature and insulated Li_2S , which is the end discharged product of S_8 in Li-S batteries[4]. Second, discharge capacity of batteries is reduced by shuttle effect of considerable amount of sulfur polymer ions (S_n^{2-}) ($3 \leq n \leq 6$) caused by shuttling between positively and negatively charged molecules [5]. Decline in battery performance is also linked with notable volume effect of elemental sulfur during charging and discharging[6].

Researchers conducted enormous work to address Li-S battery concerns, such as doping modification, coating modification, and decreasing grain size[7]. Doping modification changes crystal structure parameters to facilitate embedding and removal of Li^+ . Coating modification facilitates ionic conduction and provides specific area for electrode reactions. Decreasing grain size reduces ion diffusion distance and impedance. For its unique three-dimensional (3D) network structure and excellent physical and chemical properties[8], graphene aerogels can be used to improve the electrochemical performance of Li-S cells. Researchers in various countries carried out extensive research on preparation methods, physical principles, and other aspects of the proposed material[9]. However, no report provided details on application research of Li-S batteries. In the current paper, doping and coating were combined, and possible dual function of this combination was tested in a series of work. First, doping modification method was used to produce nitrogen-doped carbon nanotubes (NCNT) embedded in matrix, and NCNT/S reduction-oxidation graphene aerogel (RGO-gel) was prepared by hydrothermal reduction combined with freeze drying. Electrochemical tests showed that under current density of 500 mA/g, discharge specific capacity of NCNT/S(RGO-gel) remained above 912.4 mAh/g after 175 cycles. Data from current study show that doping and coating composite cathode materials can remarkably improve cycle performance of Li-S batteries.

2. EXPERIMENTAL SECTION

2.1. Preparation of 3D RGO-gel

Natural flake graphite, which was used as raw material, was placed in 20 mL 98% concentrated H_2SO_4 under ice bath conditions and magnetically stirred at 0.5 h to produce an evenly mixed solution. A total of 3.2 g $KMnO_4$ was added to the mixture, which was stirred for 2 h at 37 °C. Reaction solution (temperature control at 70 °C) was diluted with distilled water to 400 mL afterward. Appropriate amount of 5% H_2O_2 was added until the solution no longer bubbled. A total of 10 mL 5% HCL solution and large amount of deionized water were used to fully neutralize and filter materials, resulting in production of GO gel. RGO-gel was dried at 70 °C for 12 h until 0.2 g dry GO gel was produced. A certain amount of deionized water was added into 1 mg/ml GO to prepare 1 mg/ml suspensions. GO suspension was added to 50 ml polytetrafluoroethylene (PTFE) in a reaction kettle, and resulting mixture was heated to 180 °C for 12 h at heating rate of 5 °C/min. Temperature was reduced to its room value, and GO sol was obtained. GO hydrogel was precooled in refrigerator set to -20 °C for 24 h and subjected to vacuum freeze dryer at -50 °C for 48 h to produce 3D RGO-gel. RGO-gel matrix was built with Unigraphics NX software. Scheme 1 shows the preparation steps and RGO-gel-coated matrix.



Scheme 1. Main preparation process and the coated matrix for the design of RGO-gel.

2.2. Preparation of CNT/S active material

CNT and S₈ have mass ratio of 3:2. Both were placed in agate mortar and fully ground for 1 h. After stirring, materials were added to 50 ml PTFE in reaction kettle. Reaction mixture was heated in drying oven at 160 °C for 14 h to fully incorporate and spread S₈ within CNT spaces. After cooling to room temperature, active material was produced and marked as CNT/S.

2.3. Preparation of NCNT/S active material

NCNT powder, which was marked as NCNT, was prepared through high-temperature annealing (detailed procedure was reported in our previous study[10]).

S and NCNT (mass ratio of 3:2) were used to produce powdered active cathode material (black), which was marked as NCNT/S. The process was similar to CNT/S preparation.

2.4. Preparation of NCNT/S(RGO-gel) active material

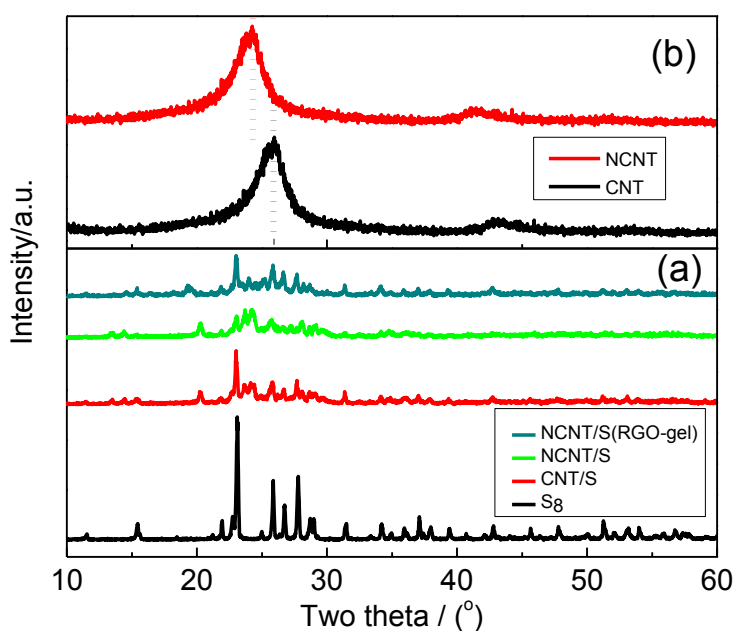


Figure 1. XRD patterns of (a) S₈, CNT/S, NCNT/S, and NCNT/S (RGO-gel) and (b) CNT, NCNT.

A certain amount of CNT/S active material was dispersed in certain volume of RGO hydrogel, which was then ultrasonically treated for 3 h at 70 °C to increase dispersion of CNT/S with gel reduction. Samples were precooled in refrigerator at -20 °C for 24 h and stored in freezer dryer for 48 h. RGO gas gel-coated material was obtained and marked as NCNT/S (RGO-gel).

3. RESULTS AND DISCUSSION

Fig. 1 displays X-ray diffraction (XRD) patterns of S₈, CNT/S, NCNT/S, and NCNT/S(RGO-gel). As shown in Fig. 1a, S₈ has many diffraction peaks at different intensities. One of the strongest diffraction peaks exists at $2\theta=23^\circ$ and shows that S₈ has good crystalline structure[11]. Diffraction peak intensity of CNT/S is lower than that of S₈; this observation resulted from enhanced overall amorphous form, which is attributed to melting of S₈ within tube gaps of CNT [12]. Diffraction pattern of NCNT/S was consistent with that of S₈ crystal, but diffraction peak intensity was obviously weaker than that of CNT/S, indicating that melted S₈ also penetrated the gaps of NCNT. After RGO-gel coating, enhancement was observed in intensity of diffraction peak of NCNT/S(RGO-gel) spectral line near $2\theta=23^\circ$. Such result is related to characteristic diffraction peaks of RGO. As shown in Fig. 1b, two typical characteristic peaks, one strong (002) and one weak (100), appeared near $2\theta=25^\circ$ and $2\theta=45^\circ$, respectively, in CNT XRD patterns[13]. These peaks are typical of CNT structures[14]. Compared with that of CNT, XRD patterns of NCNT showed spectral lines, in which diffraction peaks showed small-angle shifts. The (002) peak shift is attributed to nitrogen-doped graphite layer with enlarged spaces caused by nitrogen-doping distortion[15], whereas (100) peak shift was due to introduction of C–N bond, causing extension and distortion of the C layer of sp² orbitals[16].

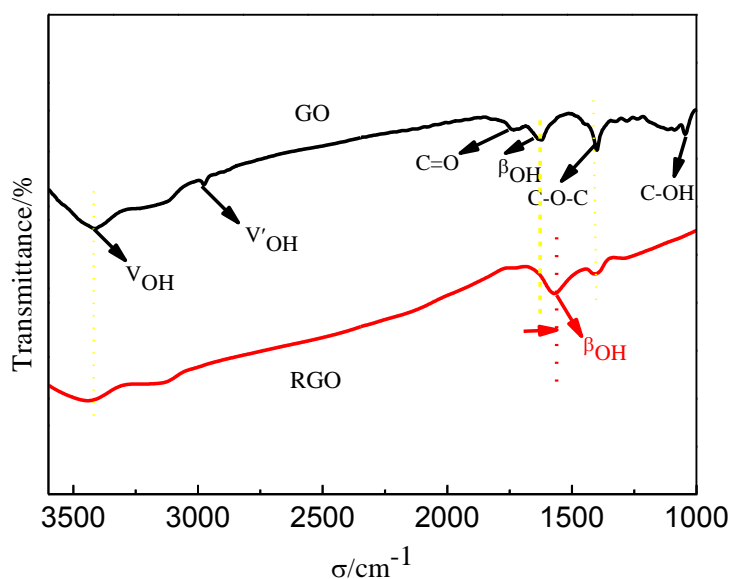


Figure 2. FTIR spectra of GO and RGO-gel.

Fig. 2. shows the Fourier transform infrared spectroscopy diagram of GO and RGO-gel. As shown in the figure, GO structure contains numerous kinds of oxygen-containing functional groups[17]. Six distinct characteristic peaks were observed at 1052, 1225, 1631, 1732, 2975, and 3430 cm^{-1} , which respectively corresponded to C–OH stretching vibration peak, C–O–C peak, OH bending vibration in water molecules, C=O stretching vibration peak, V'_{OH} (related to hydrogen bond formation), and V_{OH} stretching vibration peak. These observations were consistent with characterization results for GO[18].

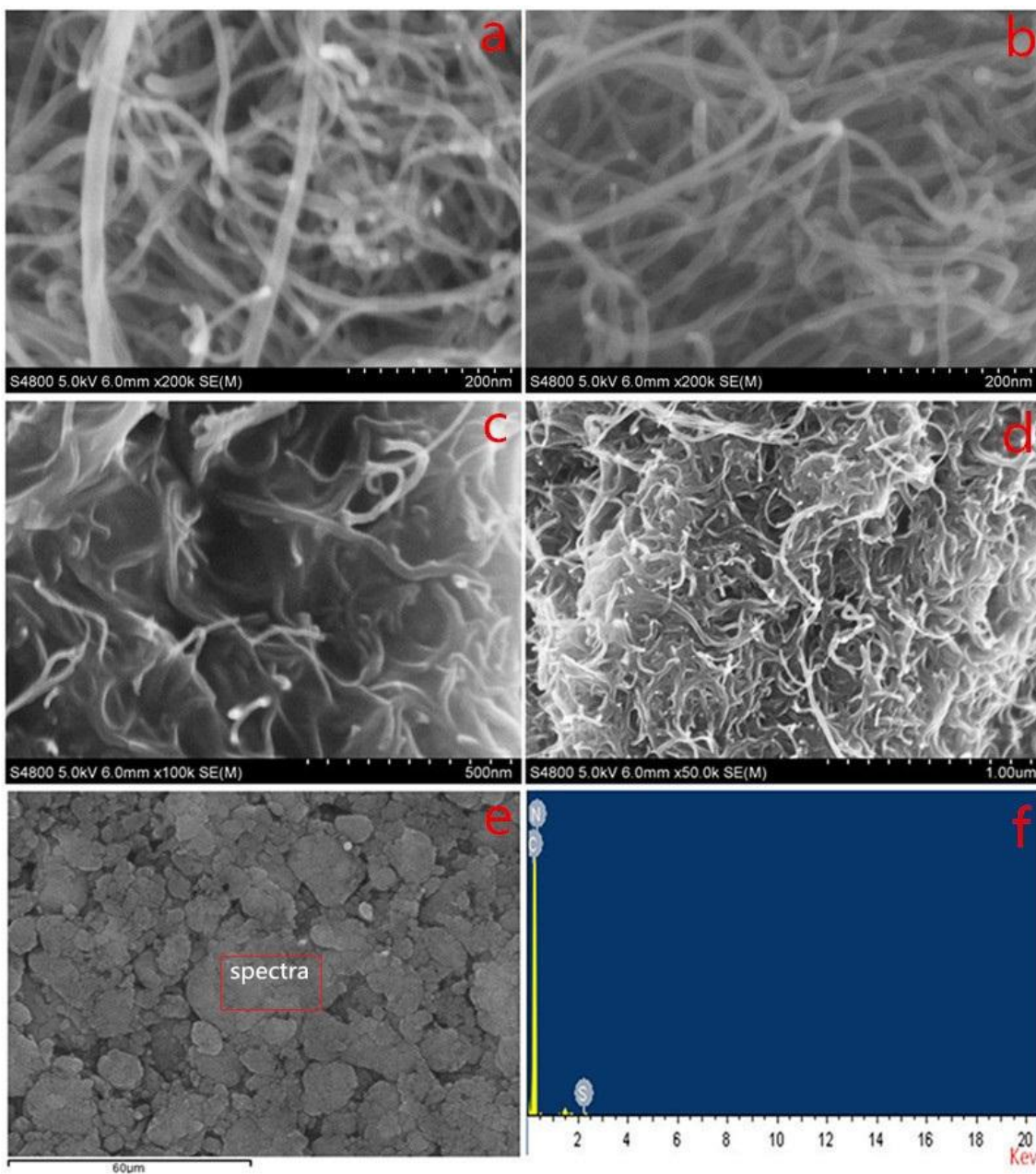


Figure 3. SEM images of (a) CNT, (b) NCNT, (c) CNT/S, (d) NCNT/S(RGO-gel), (e) low magnification SEM image and (f) EDS energy spectrum of NCNT/S(RGO-gel).

After hydrothermal reduction, compared with GO, stretching vibration peak of COH and C=O bond disappeared in 3D RGO-gel; stretching vibration peak intensity of C-O-C, V'_{OH} , and V_{OH} gradually decreased, causing gradual transformation of carbon atom structural layer into graphite and improvement in degree of order[19]. Blue shift was noted in bending vibration peak of OH in water molecules. This shift might be due to very small amount of water in test samples. Intermolecular hydrogen bonds formed among water molecules, graphene, and graphene sheets[20], whereas intramolecular hydrogen bonds formed in-between graphene sheets. Hydroxyl and carboxyl groups in graphene decreased because of hydrothermal reduction. Intramolecular and intermolecular hydrogen bonds also decreased. IR spectrum band then became wider, resulting in blue shift.

Fig. 3 shows SEM morphologies of CNT, NCNT, CNT/S, NCNT/S(RGO-gel), and *energy dispersive spectroscopy* result for NCNT. CNT diameter is 20–30 nm. CNT morphology changed slightly after nitrogen-doping, whereas morphology of NCNT was more uniform, which is convenient for full contact of electrolyte and electrode surface, as shown through comparison of Fig. 3(a) and 3(b). After nitrogen-doping, melted S_8 were fully embedded into CNT pores, as illustrated by Fig. 3(c). Overall morphology was more uniform and was absent during S_8 insertion. After reduction of GO-gas gel coating, resulting surface was smoother, and overall morphology of NCNT/S(RGO-gel) was not significantly different from that of CNT/S, as shown in Fig. 3(d). As presented in Fig. 3(f), component analysis test spectrum showed that N peak appeared near 0.4 KeV, indicating that nitrogen atoms were introduced into C network structure. Table 1 lists the results of component analysis test (Wt%).

Table 1. Component analysis test results (Wt%) of NCNT/S(RGO-gel)

Element	C	N	S	Weight
weight percentage	98.39	1.36	0.25	100
Atomic percentage	98.74	1.17	0.09	100

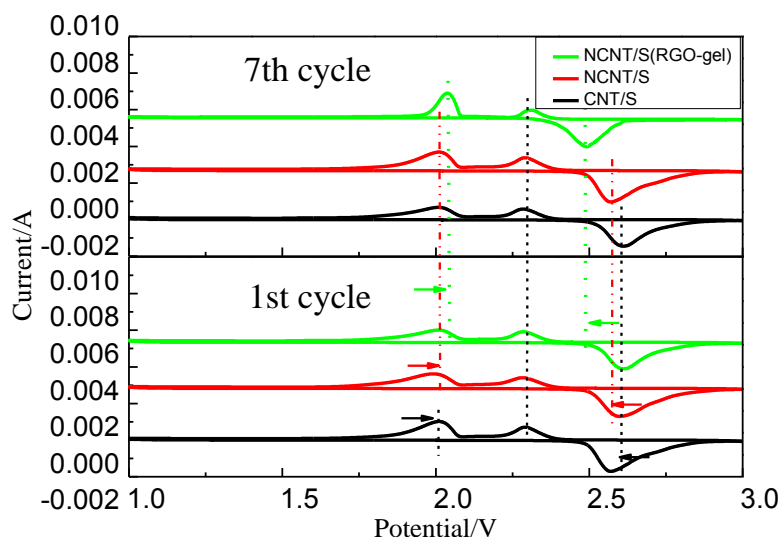


Figure 4. Capacitance–voltage curves of the batteries with composite electrode of CNT/S, NCNT/S and NCNT/S(RGO-gel) at 1st cycle and 7th cycle.

Fig. 4 displays capacitance–voltage (CV) curve of composite electrode with scanning speed of 0.0001 V/s and scanning potential of 1–3 V. The figure indicates that electrode reaction was carried out step by step. Two reduction peaks at 2.3 and 2.0 V were constantly observed during scanning from high to low voltage, respectively. Reduction peaks at 2.3 V corresponded to reduction from S₈ to Sn²⁻; other peaks at 2.0 V corresponded to further reduction from S₄²⁻ to S²⁻ (4 ≤ n ≤ 8 for peaks at both potentials). During scanning from low to high voltage, oxidation peaks were constantly observed at 2.6 V. These peaks corresponded to electrode reaction toward the direction of S₈ generation. After the seventh scan, two reduction peaks, which corresponded to positions of NCNT/S and NCNT/S(RGO-gel) electrodes, observed trends moved toward high potential values, whereas oxidation peak was noted at low potentials. Balanced NCNT/S(RGO-gel) electrode trend was more remarkable, indicating that NCNT/S and NCNT/S(RGO-gel) electrodes could maintain better capacity and prevent shuttle effect on electrodes. During electrode reaction, imbalanced was noted in two reduction peaks of CNT/S electrode without modification, and corresponding oxidation peaks shifted toward high potential values. This result further showed the inefficient reversibility of CNT/S electrode and greater difficulty in S₈ generation.

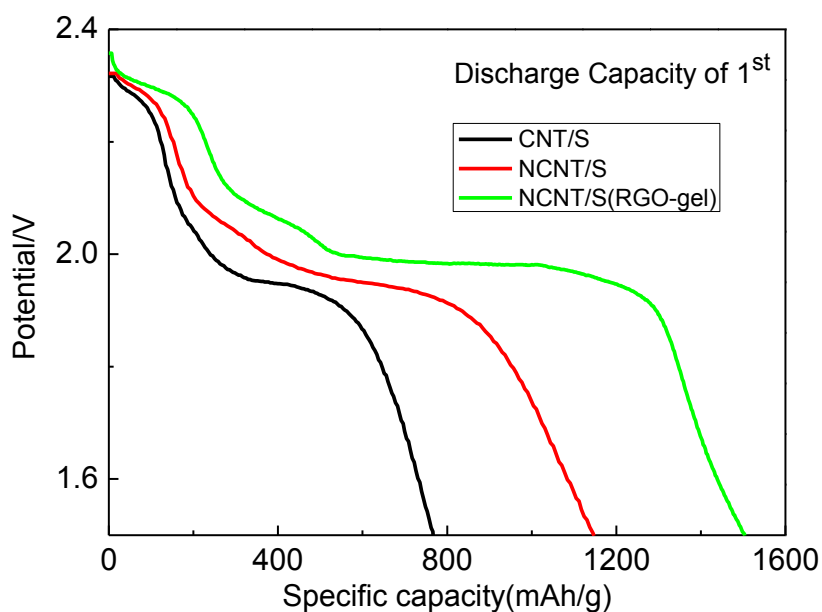
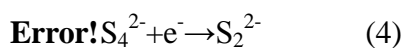
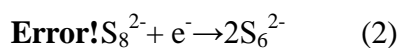
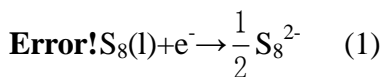
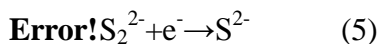


Figure 5. The initial discharge curves of the batteries with composite electrode of CNT/S, NCNT/S and NCNT/S(RGO-gel) at 500mA•g⁻¹ current density.

Fig. 5 establishes first discharge performances of different composites at current density of 500 mA•g⁻¹. Discharge curve in the graph has two discharge platforms, and given voltage is similar two reduction peaks in the CV curve. These curves are typical discharge platforms of Li–S batteries[21]. High and low voltage platforms had power values of 2.3 and 2.0 V, respectively. Corresponding electrode reactions are the following [22]:





CNT/S electrode presented first discharge specific capacity of 767 mAh•g⁻¹, whereas increases to 1147.25 and 1403.7 mAh•g⁻¹ were noted in nitrogen-doped and RGO-gel-coated material, respectively. Improvement on electrode performance resulted from nitrogen-doping, causing CNTs to scatter more easily during application. Meanwhile, lead facilitated efficient electrolyte infiltration to electrodes. RGO-gel coating layer could prevent most polysulfide Sn²⁻ (4≤n≤8) from dissolving in electrolytes. This material could then be fully utilized in electrode reaction.

The figure also shows improved discharge voltage platform, which corresponded to doped modified electrode resulting from catalytic activity of nitrogen atom in NCNT upon oxygen reduction [23], this property reduced the difficulty in electrode reaction. RGO-gel coating layer limited Sn²⁻ dissolution in electrolytes, improving discharge voltage platform after coating modification. RGO-gel coating layer extended discharge voltage platform to a certain extent and resulted in limited electrode reaction. As result, electrode material was fully involved in electrode reaction.

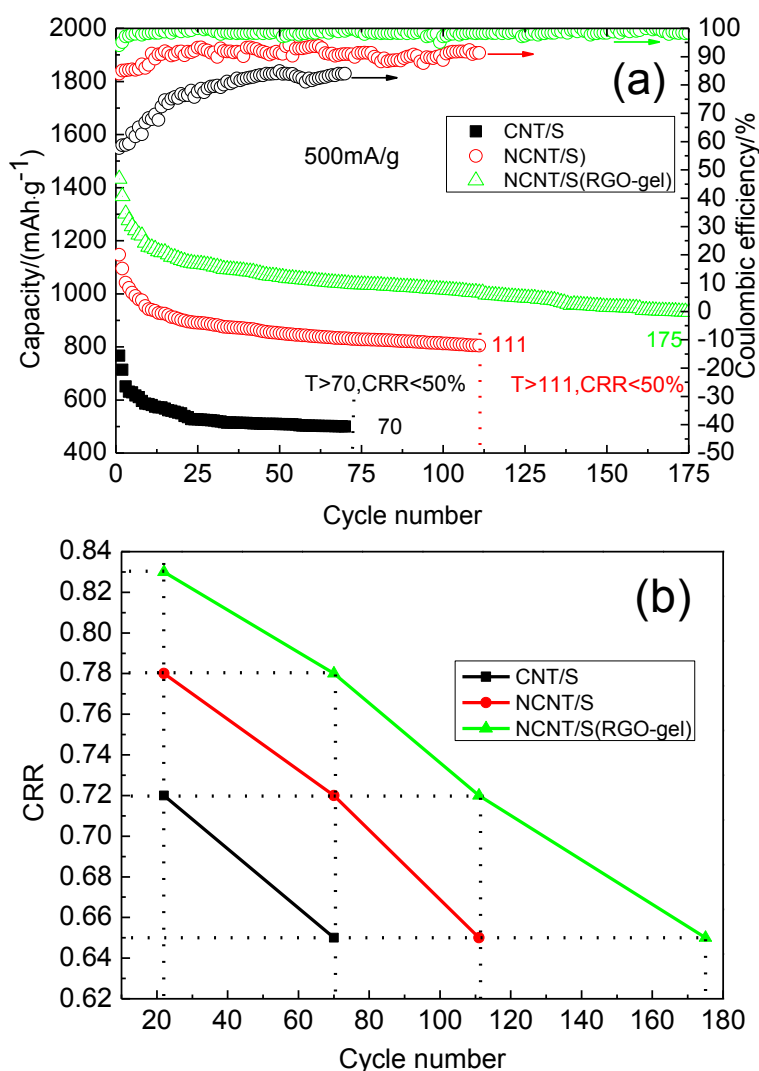


Figure 6. Cycle performance of the batteries with composite electrode of CNT/S, NCNT/S and NCNT/S(RGO-gel) (a) and capacity retention rate (b) at a current density of 500mA/g.

Fig.6 shows cycle performance of different composite electrodes under current density of 500 mA/g. CNT/S electrode displayed first discharge specific capacity of 767 mAh/g, and specific capacity was 500.05 mAh/g after 70 cycles. Capacity attenuation was very serious. Capacity retention rate (CRR) was 65%, and coulomb efficiency was 80%. Improvement was remarked on initial discharge specific capacity of electrodes, signifying good cycle performance. CRR was 72% after 70 cycles; such value was equivalent to that of modified CNT/S electrode (22 cycles). After the 111th cycle, CRR remained at 65%, and coulomb efficiency was 90%; resulting measurements were due to mixing of N atoms with CNT mesh structure in the form of N graphitic[24].

Table 2. Cycling performance of the batteries with different composite electrode

Composite electrodes	Reference	Current density	Cycling performance/ mAh•g ⁻¹
MnO ₂ /S/RGO-gel	[25]	0.1C	1360 (before cycling)
ZnO/ S/ RGO-gel	[26]	0.2C	998 (before cycling) 846 (100 cycles)
N-carbon foam/S/ RGO-gel	[27]	0.1C	913 (before cycling) 720 (50 cycles)
3D Graphene foam/S /RGO-gel	[28]	0.2C	1000 (before cycling) 645 (350 cycles)
NCNT/S(RGO-gel)	This work	500mA/g	1403 (before cycling) 912 (175 cycles)

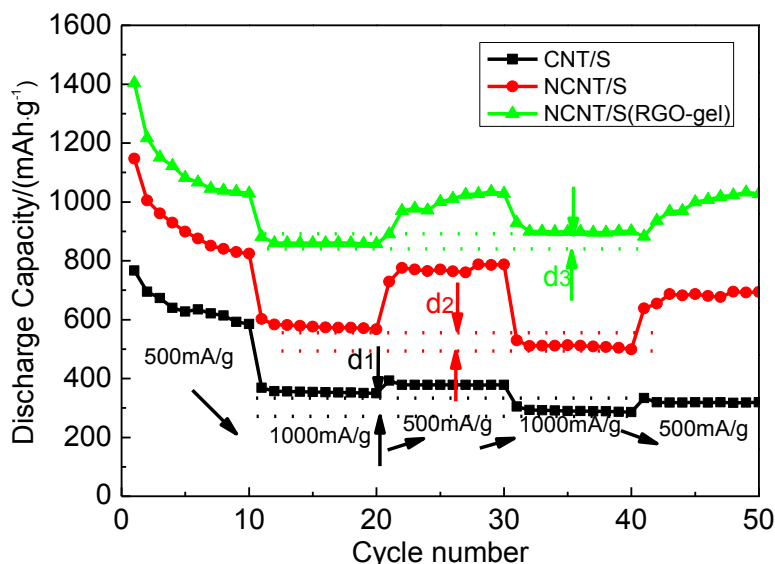


Figure 7. Rate performance of the batteries with composite electrode of CNT/S, NCNT/S and NCNT/S(S/RGO-gel).

Mixing improved conductivity of composite material, causing full participation of S₈ in electrode reaction. Test results showed the better cycle performance of (RGO-gel) electrodes than nonmodified ones. After 70 cycles, CRR was 78% and equivalent to that of uncoated modified NCNT/S electrode (22 cycles). After 111 and 175 cycles, modified electrode displayed CRR of 72% and 65%, respectively. Coulomb efficiency was sustained above 95%, showing excellent cycle performance. This result was due to strong physical adsorption function of RGO-gel. Thus, electrode

reaction was fully carried out to prevent sulfide (Sn^{2-}) loss. RGO-gel showed clear lamellar structure, which facilitated even dispersal and optimal use of active material. Information gathered presents improvement of cycle performance of batteries caused by dual effect of doping and coating modifications. As listed in Table 2, the initial discharge capacity of the battery with the composite electrode of NCNT/S(RGO-gel) possesses the highest initial discharge capacity and good cycling ability, demonstrating its excellent electrochemical performance.

Fig. 7 shows comparison of electrode rate capacities. All electrodes were tested with the following current density order: $500 \rightarrow 1000 \rightarrow 500 \rightarrow 1000 \rightarrow 500 \text{ mA/g}$. Notably, discharge capacity of doped electrode was significantly higher than that of CNT/S electrode at current density of $500 \text{ mA} \cdot \text{g}^{-1}$. After modification of RGO-gel coating, further improvement was observed in discharge capacity of electrodes. Simultaneously, proportion of active material reduced in the cathode material. Decline in capacity trend was noted in first five cycles. When discharge current density increased to $1000 \text{ mA} \cdot \text{g}^{-1}$ (at first cycle), discharge specific capacities were 857.177 and $566.7 \text{ mAh} \cdot \text{g}^{-1}$, respectively, for electrodes modified by doping and coating. These values were much larger than $349.7 \text{ mAh} \cdot \text{g}^{-1}$, which was observed for CNT/S electrode. Discharge capacity of composite electrode improved when current density was restored to $500 \text{ mA} \cdot \text{g}^{-1}$. Improvement of two electrodes was more obvious after doping and coating. However, when discharge current density was reverted to 1000 mA/g (second times), electrode modified by RGO-gel coating showed the best performance compared with first observation. Discharge specific capacity increased (as shown in Figure d3). Reduced discharge capacity was observed in CNT/S and NCNT/S electrodes modified by doping (as shown in Figure d1 and d2). This reduction was due to 3D mesh structure of RGO-gel, which can effectively fix active material. Second, such structure can be used as elastic buffer. Weakened volume effect was also detected on electrode structure. When current density was restored to $500 \text{ mA} \cdot \text{g}^{-1}$, the same phenomenon was also observed. Gathered information show that even under high current density, modified electrodes still demonstrated good stability, which was attributed to dual effect of doping and coating modification. As result, Li-S battery showed good rate performance at high current densities.

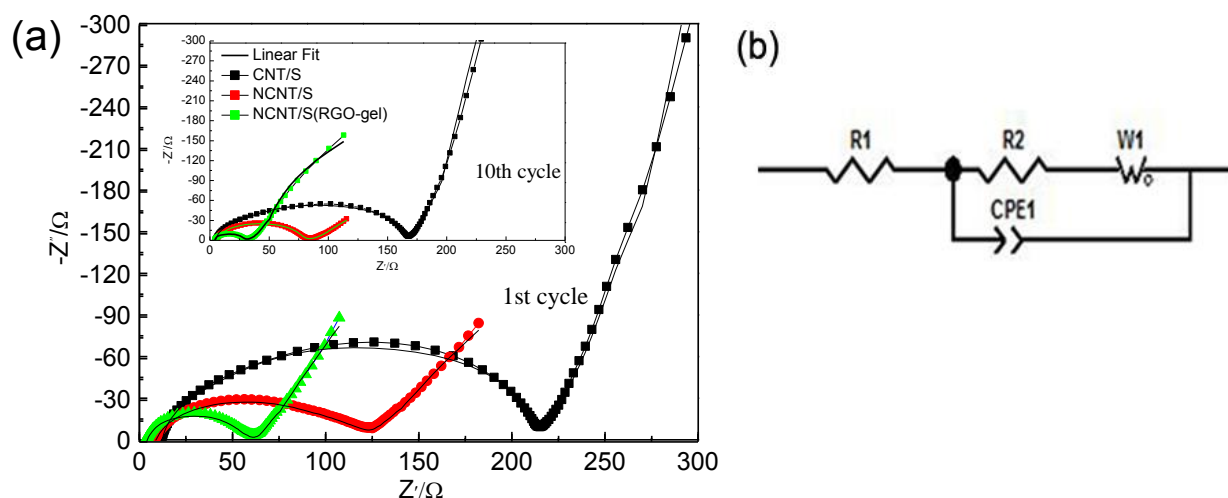


Figure 8. The AC impedance curve of the batteries with composite electrode of CNT/S, NCNT/S and NCNT/S(RGO-gel) (a) and the equivalent circuit (b).

Electrode modified by RGO-gel coating exhibited excellent discharge capacity, cycle performance, and rate performance. Fig. 8 presents electrochemical impedance spectra (EIS) of different electrodes before and after the cycles. Cycling requires charging and discharging for 10 times under current density of 500 mA/g. EIS curve is composed of three parts. Among these parts, curve and real axis Z' intercepts represent battery intrinsic impedance (resistance)[29], which was marked as R_1 ; half arc diameter of high frequency region corresponds to charge transfer resistance[30] (R_2); low frequency region at horizontal axis and 45-degree diagonal (Warburg impedance, marked as Z_w)[31] correspond to diffusion impedance of Li^+ in electrolyte. Fig. 9 shows the curve of low frequency region Z' at $\omega^{-0.5}$. The following shows the formula for lithium-ion diffusion coefficient (D) measured by *alternating current* impedance method[32]:

$$D = 0.5 \frac{R_g}{n^2 F^2 C} \frac{1}{Z_w} \quad Z_{re} = R_s + R_{ct} + \sigma W^{-1/2}$$

where D is diffusion coefficient of Li^+ in electrodes, and n is number of electrons transferred by electrode reaction. R is gas constant ($8.314 \text{ J mol}^{-1} \text{ K}^{-1}$), T is thermodynamic temperature (301.5 K), A is electrode area in electrolyte, and F is Faraday constant (96500 C mol^{-1}). C is molar concentration of Li^+ in the material (one Li_2S in unit cell exists in $6Li^+$ and $3S^{2-}$, Avogadro's constant $N_A = 6.02 \times 10^{23}$ atoms/molecules); σw is diffusion coefficient of Z_w in frequency range between 0.01–0.1 Hz, linear fitting of $Z_w^{-0.5}$ (Z' is real part of Z_w , w is angular frequency). σw was obtained for three groups of electrodes. ZView software was used to fit EIS of different electrodes before and after cycling. Table 2 provides fitting values obtained from equivalent circuit diagram.

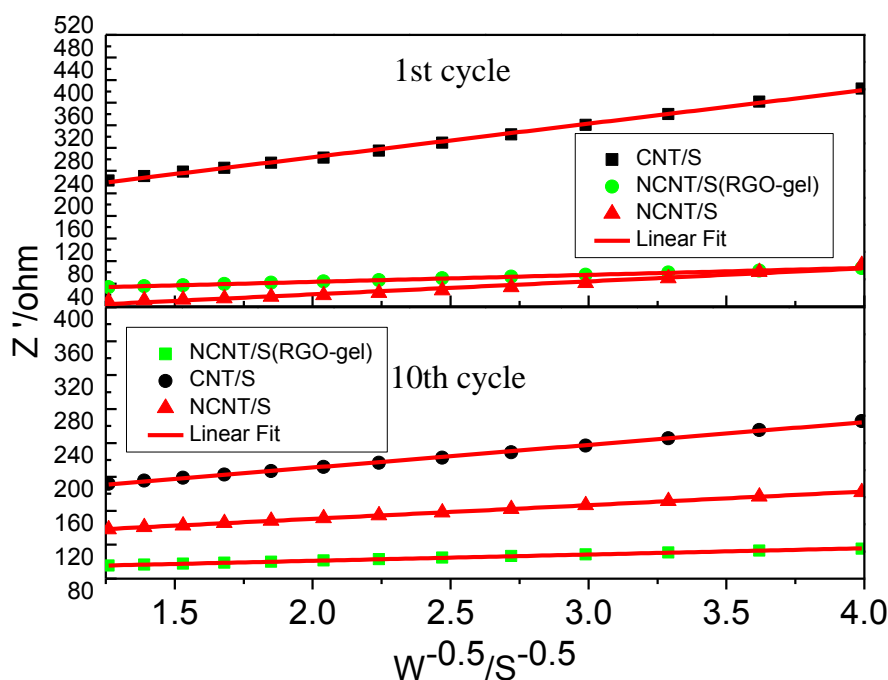


Figure 9. The relationship between the low frequency region Z' and $w^{-0.5}$ of the batteries with composite electrode of CNT/S, NCNT/S and NCNT/S(RGO-gel).

R_2 and Z_w of NCNT/S electrode were significantly less than those of CNT/S electrode. Decreased R_2 was due to doping modification, which not only changed local charge density but also enhanced electron transfer of CNT. Decreased Z_w indicated that introduction of nitrogen atoms reduced resistance of Li^+ diffusion in electrolyte. R_2 and Z_w were further reduced after modification of RGO-gel coating. RGO-gel demonstrated good conductive properties, and RGO-gel coating layer provided specific reaction space, which improved utilization of active material. Change was not observed in electrodes with inherent impedance of battery R_1 after 10 cycles. R_2 and Z_w of resistance were less than those observed before the cycle; such values were consistent with IS. Active substance was completely penetrated by electrolytes after 10 cycles, reducing diffusion resistance of Li^+ . Diffusion coefficient in Table 3 also indicates that when electrode was discharged at high current density, optimum discharge capacity was observed for electrode modified by RGO-gel. NCNT/S electrode displayed better discharge capacity than CNT/S. This result was consistent with rate capability of composite material, as shown in Fig 7.

Table 3. Kinetic parameters of the batteries with composite electrode of CNT/S, NCNT/S and NCNT/S(RGO-gel)

Sample	CNT/S		NCNT/S		NCNT/S(RGO-gel)	
	1st	10th	1st	10th	1st	10th
$R_1(\Omega)$	10.72	10.19	5.124	5.009	3.909	3.87
$R_2(\Omega)$	198.8	80.261	45.83	39.32	6.46	3.46
$Z_w(\Omega)$	133.3	77.6	43.17	37.27	6.17	2.76
$\sigma_w(\Omega\text{cm}^2\text{s}^{-0.5})$	59.39735	26.76857	23.05054	16.1078	12.37813	7.41266
$D(\text{cm}^2/\text{s})$	2.7673E-12	1.3624E-11	1.8373E-11	3.7624E-11	6.3714E-11	1.7766E-8

4. CONCLUSIONS

NCNT/S (RGO-gel) was obtained by combining doping and coating modification methods. Results showed that when current density was $500 \text{ mA}\cdot\text{g}^{-1}$, discharge specific capacity of NCNT/S(RGO-gel) electrode was maintained at 912.4 mAh/g after 175 cycles. When current density was tested under the condition of $500 \rightarrow 1000 \rightarrow 500 \rightarrow 1000 \rightarrow 500 \text{ mA/g}$, discharge specific capacity of NCNT/S(RGO-gel) electrodes could still be restored to 1027.77 mAh/g. Even under high current density, modified electrodes still showed good stability. Thus, Li-S cells demonstrated good rate performance. Data showed that doping and coating improved electrochemical performance of composite cathode material.

CONFLICT OF INTERESTS

The authors declare that there is no conflict of interests regarding the publication of this paper.

ACKNOWLEDGEMENTS

This work is financially sponsored in part by Natural Science Foundation of China (Grant No. 11364011). Part of this work was supported by Natural Science Foundation of China (Grants No. 51002029).

References

1. Y. Sun, G. Li, Y. Lai, D. Zeng and H. Cheng, *Sci Rep*, 6 (2016) 22048.
2. H.H. Deng, L.B. Yao, Q.A. Huang, Q.M. Su, J. Zhang and G.H. Du, *Materials Research Bulletin*, 84 (2016) 218-224.
3. S.T. Seyyedini, M.R. Sovizi and M.R. Yaftian, *Chemical Papers*, 70 (2016) 1590-1599.
4. D.W. Rao, Y.H. Wang, L.Y. Zhang, S.S. Yao, X.Y. Qian, X.M. Xi, K.S. Xiao, K.M. Deng, X.Q. Shen and R.F. Lu, *Carbon*, 110 (2016) 207-214.
5. X.R. Zhang, W. Ooki, Y.R. Kosaka, A. Okonogi, G. Marzun, P. Wagener, S. Barcikowski, T. Kondo and J. Nakamura, *Applied Surface Science*, 389 (2016) 911-915.
6. Y. Li, J. Yao, Y. Zhu, Z. Zou and H. Wang, *Journal of Power Sources*, 203 (2012) 177-183.
7. W. Liu, Z. Chen, G. Zhou, Y. Sun, H.R. Lee, C. Liu, H. Yao, Z. Bao and Y. Cui, *Advanced Materials*, 28 (2016) 3578-3583.
8. C.H. Tang, X.S. Yin and H. Gong, *Electrochimica Acta*, 114 (2013) 543-550.
9. T. Soltani and B.K. Lee, *Chemical Engineering Journal*, 306 (2016) 204-213.
10. J. Xiao, H. Wang, Y. Hou and Y. Guo, *RSC Adv.*, 6 (2016) 38943-38949.
11. G.V. Lau, P.A. Hunt, E.A. Muller, G. Jackson and I.J. Ford, *Journal of Chemical Physics*, 143 (2015).
12. M.V.D. Prasad and B. Bhattacharya, *Journal of Applied Physics*, 118 (2015).
13. N.G. Moreno, D. Gervasio, A.G. Garcia and J.F.P. Robles, *Journal of Power Sources*, 300 (2015) 229-237.
14. S. Moon, Y.H. Jung, W.K. Jung, D.S. Jung, J.W. Choi and D.K. Kim, *Adv Mater*, 25 (2013) 6547-6553.
15. Q. Tang, D. Wang, D.M. Yao, C.W. Yang and Y.C. Sun, *Water Sci Technol*, 73 (2016) 1652-1658.
16. Y. Liu, D. Lin, Z. Liang, J. Zhao, K. Yan and Y. Cui, *Nat Commun*, 7 (2016) 10992.
17. M. Aadil, W. Shaheen, M.F. Warsi, M. Shahid, M.A. Khan, Z. Ali, S. Haider and I. Shakir, *J Alloy Compd*, 689 (2016) 648-654.
18. F. Tan, L.C. Cong, N.M. Saucedo, J.S. Gao, X.N. Li and A. Mulchandani, *J Hazard Mater*, 320 (2016) 226-233.
19. Q.F. Shi, M. Chen and G.W. Diao, *Electrochim Acta*, 114 (2013) 693-699.
20. J.X. Ma, T.M. Wang and X.S. Lu, *Pak J Bot*, 45 (2013) 2043-2050.
21. D.N. Fronczek and W.G. Bessler, *J Power Sources*, 244 (2013) 183-188.
22. G. He, S. Evers, X. Liang, M. Cuisinier, A. Garsuch and L.F. Nazar, *Acs Nano*, 7 (2013) 10920-10930.
23. D. Lin, Y. Liu, Z. Liang, H.W. Lee, J. Sun, H. Wang, K. Yan, J. Xie and Y. Cui, *Nat nanotechnol*, 11 (2016) 626-632.
24. J.E. Kim, J. Lim, G.Y. Lee, S.H. Choi, U.N. Maiti, W.J. Lee, H.J. Lee and S.O. Kim, *Acs Appl Mater Inter*, 8 (2016) 1571-1577.
25. X. Zhao, H. Wang, G. Zhai and G. Wang, *Chemistry*, 23 (2017) 7037-7045.
26. M. Yu, A. Wang, F. Tian, H. Song, Y. Wang, C. Li, J.D. Hong and G. Shi, *Nanoscale*, 7 (2015) 5292-5298.
27. M. Xiang, L. Yang, Y. Zheng, J. Huang, P. Jing, H. Wu, Y. Zhang and H. Liu, *J. Mater. Chem. A*, 5 (2017) 18020-18028.
28. G. Hu, C. Xu, Z. Sun, S. Wang, H.M. Cheng, F. Li and W. Ren, *Adv Mater*, 28 (2016) 1603-1609.

29. C. Melero, A. Guijarro, V. Baumann, A.J. Perez-Jimenez and M. Yus, *Eur J Org Chem*, (2007) 5514-5526.
30. S. Wang, Q.H. Zhu, X.Y. Guo, Y.J. Gui, J.D. Bao, C. Helliwell and L.J. Fan, *Febs Letters*, 581 (2007) 4789-4793.
31. U.B. Demirci, *Electrochim Acta*, 53 (2007) 737-739.
32. X.Y. Zhao, J.P. Tu, Y. Lu, J.B. Cai, Y.J. Zhang, X.L. Wang and C.D. Gu, *Electrochim Acta*, 113 (2013) 256-262.

© 2017 The Authors. Published by ESG (www.electrochemsci.org). This article is an open access article distributed under the terms and conditions of the Creative Commons Attribution license (<http://creativecommons.org/licenses/by/4.0/>).